Experimental Constraints on Quaternary Structure in Alzheimer's β-Amyloid Fibrils†

Aneta T. Petkova,‡ Wai-Ming Yau, and Robert Tycko*

Laboratory of Chemical Physics, National Institute of Diabetes and Digestive and Kidney Diseases, National Institutes of Health, Bethesda, Maryland 20892-0520

Received September 27, 2005; Revised Manuscript Received November 15, 2005

ABSTRACT: We describe solid-state nuclear magnetic resonance (NMR) measurements on fibrils formed by the 40-residue β-amyloid peptide associated with Alzheimer's disease ($A\beta_{1-40}$) that place constraints on the identity and symmetry of contacts between in-register, parallel β-sheets in the fibrils. We refer to these contacts as internal and external quaternary contacts, depending on whether they are within a single molecular layer or between molecular layers. The data include (1) two-dimensional ^{13}C-^{13}C NMR spectra that indicate internal quaternary contacts between side chains of L17 and F19 and side chains of I32, L34, and V36, as well as external quaternary contacts between side chains of I31 and G37; (2) two-dimensional ^{15}N-^{13}C NMR spectra that indicate external quaternary contacts between the side chain of M35 and the peptide backbone at G33; (3) measurements of magnetic dipole−dipole couplings between the side chain carboxylate group of D23 and the side chain amine group of K28 that indicate salt bridge interactions. Isotopic dilution experiments allow us to make distinctions between intramolecular and intermolecular contacts. On the basis of these data and previously determined structural constraints from solid-state NMR and electron microscopy, we construct full molecular models using restrained molecular dynamics simulations and restrained energy minimization. These models apply to $A\beta_{1-40}$ fibrils grown with gentle agitation. We also present evidence for different internal quaternary contacts in $A\beta_{1-40}$ fibrils grown without agitation, which are morphologically distinct.

Amyloid fibrils are filamentous aggregates formed by a wide variety of peptides and proteins and distinguished from other types of protein fibrils by their appearance in electron microscope (EM)[1] images, by their dye-binding properties, and by the presence of cross-β structural motifs within the fibrils (*1*, *2*). Amyloid fibrils are likely causative or contributing agents in diseases such as Alzheimer's disease, type 2 diabetes, Parkinson's disease, and transmissible spongiform encephalopathies (*3*). The formation and transmission of several prions in yeast and fungi are known to be based on the formation of amyloid fibrils by particular proteins (*4*). Many proteins that are not known to form amyloid fibrils in vivo can also form amyloid fibrils in vitro under conditions that destabilize their unaggregated states (*5*, *6*).

Determination of the full molecular structures of amyloid fibrils requires unusual experimental approaches, due to their inherent noncrystalline, insoluble nature (*2*). Full structure determination requires experimental constraints at the primary, secondary, tertiary, and quaternary structural levels (*7*). As for monomeric peptides and proteins, primary and secondary structures refer to the amino acid sequence and to segments with standard backbone conformations, respectively. In the case of amyloid fibrils, β-strands are the predominant secondary structural elements. Helical segments have not yet been detected in the core structures of amyloid fibrils. Experimental determination of secondary structure in amyloid fibrils therefore consists of the identification of structurally ordered and disordered segments, and the identification of β-strand and non-β-strand segments (i.e., loops, bends, or turns). Solid-state nuclear magnetic resonance (NMR) (*8*−*19*), hydrogen/deuterium (H/D) exchange (*14*, *20*−*27*), proline-scanning mutagenesis (*28*, *29*), electron paramagnetic resonance (EPR) (*30*−*32*), and infrared and Raman spectroscopies (*33*, *34*) have been applied to the problem of secondary structure determination. Tertiary structure in amyloid fibrils can be defined as the organization of β-strand segments into parallel or antiparallel β-sheets, with a specific registry of interstrand hydrogen bonds within the β-sheets. Solid-state NMR (*7*, *8*, *11*, *15*, *16*, *19*, *35*−*44*) and EPR (*30*−*32*, *45*, *46*) measurements have been particularly useful in experimental determinations of tertiary structure.

Quaternary structure in amyloid fibrils can then be defined as the positions and orientations of β-sheets relative to one another. As demonstrated by X-ray fiber diffraction (*1*, *33*, *47*, *48*), EM (*49*), and solid-state NMR (*50*) data, the β-sheets

† This work was supported by the Intramural Research Program of the National Institute of Diabetes and Digestive and Kidney Diseases of the National Institutes of Health.

* Corresponding author: Dr. Robert Tycko, National Institutes of Health, Building 5, Room 112, Bethesda, MD 20892-0520. Phone: 301-402-8272. Fax: 301-496-0825. E-mail: robertty@mail.nih.gov.

‡ Current address: Department of Physics, University of Florida, Gainesville, FL 32611.

[1] Abbreviations: EM, electron microscopy; NMR, nuclear magnetic resonance; H/D, hydrogen/deuterium; EPR, electron paramagnetic resonance; $A\beta_{1-40}$, 40-residue β-amyloid peptide; MPL, mass-per-length; 2D, two-dimensional; MAS, magic-angle spinning; REDOR, rotational echo double resonance; TEDOR, transferred echo double resonance; MD, molecular dynamics; HET-$s_{218-289}$, residues 218−289 of the HET-s protein.

10.1021/bi051952q
Published on Web 12/17/2005

in amyloid fibrils have a cross-β orientation, meaning that the β-strand segments run approximately perpendicular to the long axes of the fibrils, while the interstrand hydrogen bonds are directed approximately parallel to the long axes. As represented in recent models for amyloid structures (*7*, *10*, *14*, *29*, *36*, *42*, *44*, *51*−*59*) and supported by recent X-ray crystal structures of short amyloid-forming peptides (*60*), the core of an amyloid fibril contains two or more layers of β-sheets. The quaternary structure is dictated by a set of contacts among amino acid side chains that project from adjacent β-sheets. In fibrils formed by relatively long peptides (or by bona fide proteins), the adjacent β-sheets may be formed either by β-strands from the same peptide molecules or by β-strands from different molecules. Thus, the side chain contacts that dictate quaternary structure may be either intramolecular or intermolecular.

In the case of fibrils formed by the 40-residue β-amyloid peptide associated with Alzheimer's disease (Aβ_{1-40}), solid-state ^{13}C NMR chemical shifts and line widths indicate that residues 1−9 are structurally disordered, residues 10−22 and 30−40 form β-strands (with enhanced disorder at the C-terminus and in the vicinity of residues 14−16 for fibrils grown with gentle agitation), and residues 23−29 form a bend or loop (*10*, *11*). The two β-strands form two separate in-register, parallel β-sheets (*37*, *38*), which can make contact with one another because of the intervening bend segment (*9*). This description of secondary and tertiary structure in Aβ_{1-40} fibrils is generally consistent with EPR (*32*), proline-scanning mutagenesis (*29*), proteolysis (*61*, *62*), and hydrogen exchange (*20*, *27*) data. Secondary and tertiary structural differences between models derived from solid-state NMR data (*7*, *10*) and from other data (*29*, *52*) are largely attributable to differences in the information content of the various techniques and their sensitivity to structural disorder, as discussed below.

Experimental determination of quaternary structure in amyloid fibrils has been comparatively difficult. In most models, quaternary contacts and quaternary structure have been chosen in the absence of direct experimental constraints. In the case of Aβ_{1-40} fibrils, information about quaternary contacts was obtained recently by Shivaprasad et al. (*52*), who performed disulfide cross-linking experiments on double cysteine mutants of Aβ_{1-40}. Fibrils formed by the L17C/L34C mutant (initially in the reduced state) were oxidatively cross-linked most rapidly and efficiently, suggesting a quaternary structure in which side chains of L17 and L34 are in proximity. L17C/L34C, L17C/M35C, and L17C/V36C mutants were all found to be capable of forming amyloid fibrils after oxidation in their monomeric states, suggesting that other quaternary structures for Aβ_{1-40} fibrils are also possible (*52*). This result is consistent with the molecular-level polymorphism of Aβ_{1-40} fibrils revealed by our own recent solid-state NMR and EM experiments (*11*).

In related work, Sciaretta et al. have shown that Aβ_{1-40} with a lactam cross-link between D23 and K28 forms amyloid fibrils significantly more rapidly than the wild-type peptide, with no detectable lag phase in the fibrillization kinetics (*43*). The lactam cross-linking experiments are consistent with the observation by solid-state NMR of a salt bridge interaction between side chains of D23 and K28 in fibrils formed with gentle agitation (*10*, *11*). The absence or partial population of this salt bridge in fibrils formed under purely quiescent conditions (*11*) is another specific structural indication of molecular-level polymorphism in Aβ_{1-40} fibrils.

In this paper, we describe new solid-state NMR measurements on Aβ_{1-40} fibrils that provide direct constraints on quaternary structure. Most of the data presented below were obtained on fibrils grown with gentle agitation (or from seeds that were grown with gentle agitation, as previously described (*11*)). Mass-per-length (MPL) measurements by scanning transmission electron microscopy have shown that the basic structural unit in these fibrils contains two layers of Aβ_{1-40} molecules in a cross-β motif (*7*, *11*). Data described above indicate that each layer of molecules consists of two β-sheet layers. Thus, the protofilament (i.e., the experimentally observed structural unit with minimum MPL) in agitated Aβ_{1-40} fibrils is a four-layered β-sheet structure with both "internal" and "external" quaternary contacts, as depicted in Figure 1. Internal contacts are those between β-sheets within a single molecular layer, while external contacts are those between β-sheets in different molecular layers. The data presented below indicate internal quaternary contacts between side chains of L17 and F19 and side chains of I32, L34, and V36, external quaternary contacts between the side chain of I31 and the peptide backbone at G37, and external quaternary contacts between the side chain of M35 and the peptide backbone at G33. These data support the C_{2z} quaternary structure in Figure 1a, with the F19/L34 peptide conformation in Figure 1b.

In addition, we present limited data for Aβ_{1-40} fibrils grown under quiescent conditions. These data provide additional evidence that the internal quaternary contacts in agitated and quiescent fibrils are different. Finally, we report the results of isotopic dilution experiments, in which fibrils were grown from mixtures of ^{15}N,^{13}C-labeled and unlabeled peptides. The effects of isotopic dilution permit distinctions between intramolecular and intermolecular contacts to be made, with implications for the alignment of internal quaternary contacts and the resemblance of amyloid fibril structures to those of β-helical proteins.

MATERIALS AND METHODS

Sample Preparation. Aβ_{1-40} peptides were synthesized, purified, and fibrillized exactly as previously described (*11*). The amino acid sequence is DAEFRHDSGY EVHHQKLVFF AEDVGSNKGA IIGLMVGGVV. Fibrils were grown at 22 ± 2 °C, with 210 μM peptide concentration, 10 mM sodium phosphate buffer, pH 7.4, and 0.01% NaN_3. Initial dissolution of Aβ_{1-40} in buffer and pH adjustment were performed as described, leading to fibril structures that were reproducible and independent of sample-to-sample variations in the initial state of the purified peptide. Parent fibrils were grown either with gentle rotary agitation in horizontal polypropylene tubes or in quiescent dialysis tubes suspended in buffer. Growth of daughter fibrils from seeds (i.e., from sonicated fragments of agitated or quiescent parent fibrils) was carried out in dialysis tubes. As shown by Petkova et al., seeded growth leads to self-propagation of both fibril morphology as seen by EM and fibril structure as seen by solid-state NMR (*11*). The structural homogeneity of all fibril samples was verified by both EM and solid-state ^{13}C NMR.

Samples were synthesized with uniformly ^{15}N,^{13}C-labeled residues at selected positions that were chosen to maximize

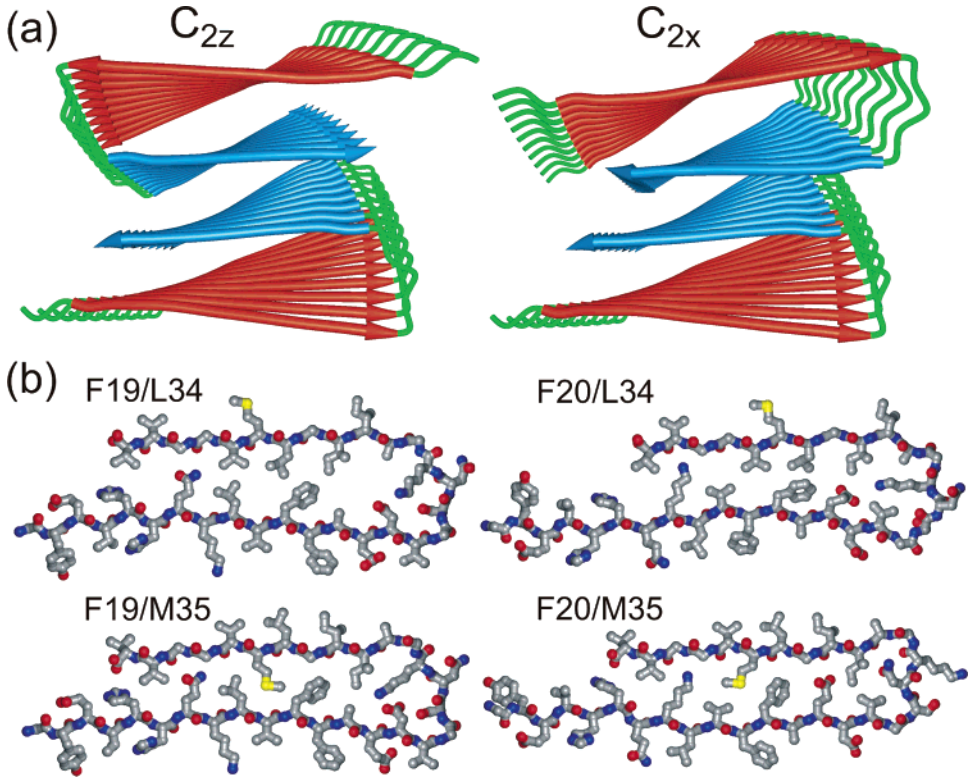

FIGURE 1: (a) Cartoon representations of candidate quaternary structures for Aβ_{1-40} fibrils with either C_{2z} or approximate local C_{2x} symmetries. The *z* axis is the long axis of the fibril, approximately perpendicular to the page. The *x* axis is perpendicular to *z* and approximately parallel to the β-strands. Each Aβ_{1-40} molecule contains two β-strands, colored red (N-terminal β-strand) and blue (C-terminal β-strand), which form separate, parallel β-sheets. Different quaternary structures are distinguished by different sets of side chain contacts at the "internal" interfaces (between a red and a blue β-sheet) and the "external" interface (between two blue β-sheets). (b) Four possible molecular conformations that lead to different quaternary structures. Quaternary contacts at the internal interface are between F19 and L34, F20 and L34, F19 and M35, or F20 and M35. Residues 1−8 are conformationally disordered and are omitted.

Table 1: Isotopic Labeling of Aβ_{1-40} Fibril Samples

sample name	uniformly ^{15}N, ^{13}C-labeled residues	labeled fraction[a] (%)
Aβ_{1-40}-L1	K16, F19, A21, E22, I32, V36	100
Aβ_{1-40}-L1d	K16, F19, A21, E22, I32, V36	31
Aβ_{1-40}-L2	F19, V24, G25, A30, I31, L34, M35	100
Aβ_{1-40}-L3	F20, E22, K28, I32, M35, V36	100
Aβ_{1-40}-L4	F20, D23, V24, K28, G29, A30, I31	100
Aβ_{1-40}-L4d	F20, D23, V24, K28, G29, A30, I31	33
Aβ_{1-40}-L5	I31, G33, M35, G37, V39	100
Aβ_{1-40}-L5d	I31, G33, M35, G37, V39	33

[a] Mole fraction of labeled peptide molecules when fibrils were grown from a mixture of labeled and unlabeled molecules. Labeled molecules have >95% isotopic enrichment at all nitrogen and carbon sites of the indicated residues. Unlabeled molecules have natural-abundance levels of ^{15}N and ^{13}C.

spectral resolution in two-dimensional (2D) ^{13}C NMR spectra and to permit searches for particular quaternary contacts. Labeled positions for samples used in the experiments described below are listed in Table 1.

Except as noted below, solid-state NMR measurements were carried out on lyophilized fibrils, prepared by centrifugation of the fibril growth solutions, removal of the supernatant, and resuspension of fibrils in deionized water prior to lyophilization. Lyophilized and fully hydrated fibrils exhibit identical ^{13}C NMR chemical shifts, indicating that lyophilization does not perturb the molecular structure of the fibrils. Lyophilization allowed larger sample quantities to be packed into the magic-angle spinning (MAS) NMR rotors and higher MAS frequencies to be achieved, as required by the measurements.

Solid-State NMR Spectroscopy. Experiments were performed at 9.39 and 14.1 T fields (100.4, 100.8, and 150.6 MHz ^{13}C NMR frequencies) using Varian Infinity and InfinityPlus spectrometers and Varian MAS probes with 3.2 mm diameter MAS rotors. Experiments were performed at room temperature. Rotors typically contained 5−10 mg of lyophilized Aβ_{1-40} fibrils compressed into a solid plug, with Teflon spacers to contain the fibrils in the center of the NMR detection coil for better radio frequency (rf) field homogeneity. Proton decoupling fields were typically 110 kHz, with two-pulse phase modulation (*63*) during chemical shift evolution periods in all pulse sequences.

Quaternary contacts between pairs of ^{13}C-labeled sites were detected as cross-peaks in 2D ^{13}C-^{13}C NMR spectra obtained in a 14.1 T field, with MAS frequencies from 16.60 to 23.50 kHz and mixing periods from 500 to 1500 ms. In experiments to detect contacts between phenylalanine residues and residues containing methyl groups, the MAS frequency was deliberately set near the difference between NMR frequencies of aromatic and methyl carbons to enhance aromatic-to-methyl spin polarization transfers by the rotational resonance effect (*64*). In some measurements, a proton rf field equal to the MAS frequency was applied during the mixing period (*65*, *66*). Presence or absence of this proton rf field did not affect cross-peak intensities significantly with the very long mixing periods employed in these measurements. 2D spectra were obtained in 48−96 h with a 2 s recycle delay.

Salt bridge interactions between D23 and K28 side chains were detected through measurements of ^{15}N-^{13}C nuclear magnetic dipole−dipole couplings with the frequency-

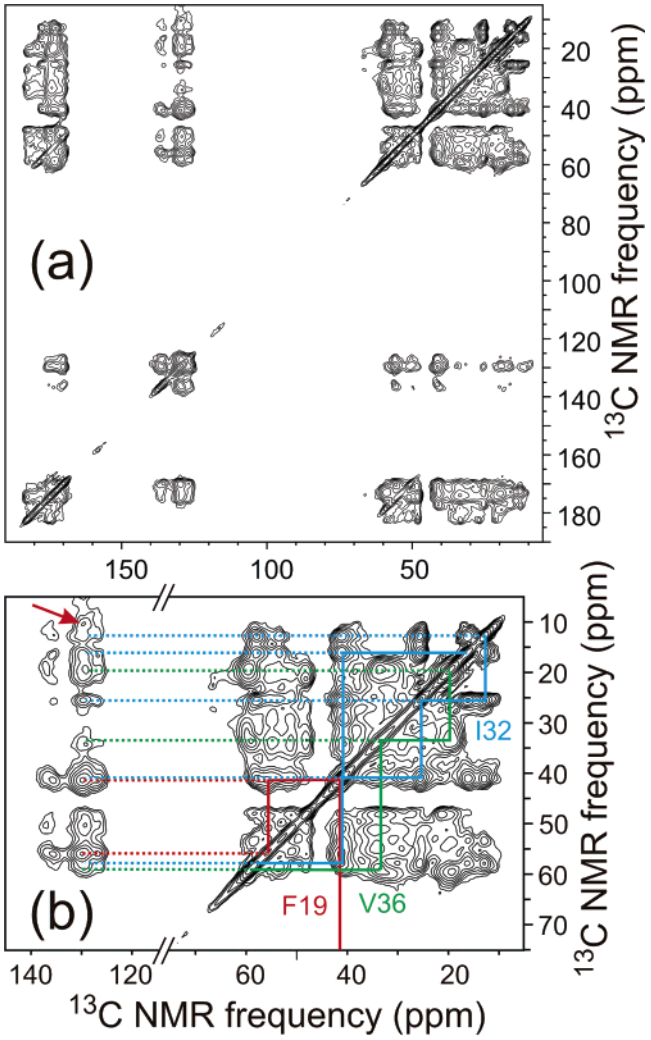

FIGURE 2: (a) 2D solid-state ^{13}C-^{13}C NMR spectrum of Aβ_{1-40}-L1 fibrils, recorded at 14.1 T with a 500 ms mixing period and 18.00 kHz MAS frequency. Strongest cross-peaks connect all NMR frequencies of a given ^{13}C-labeled residue. Weaker cross-peaks connect NMR frequencies of ^{13}C-labeled residues that make quaternary contacts or are sequential. (b) Expansion of aliphatic/aliphatic and aliphatic/aromatic regions. Solid lines trace resonance assignment paths for aliphatic ^{13}C NMR frequencies of F19, I32, and V36. Dotted lines connect aliphatic frequencies of these residues to the aromatic ^{13}C NMR signal of F19 at 129.5 ppm. Aliphatic/aromatic cross-peaks indicate F19/I32 and F19/V36 side chain contacts. Red arrow points to an MAS sideband cross-peak of F19.

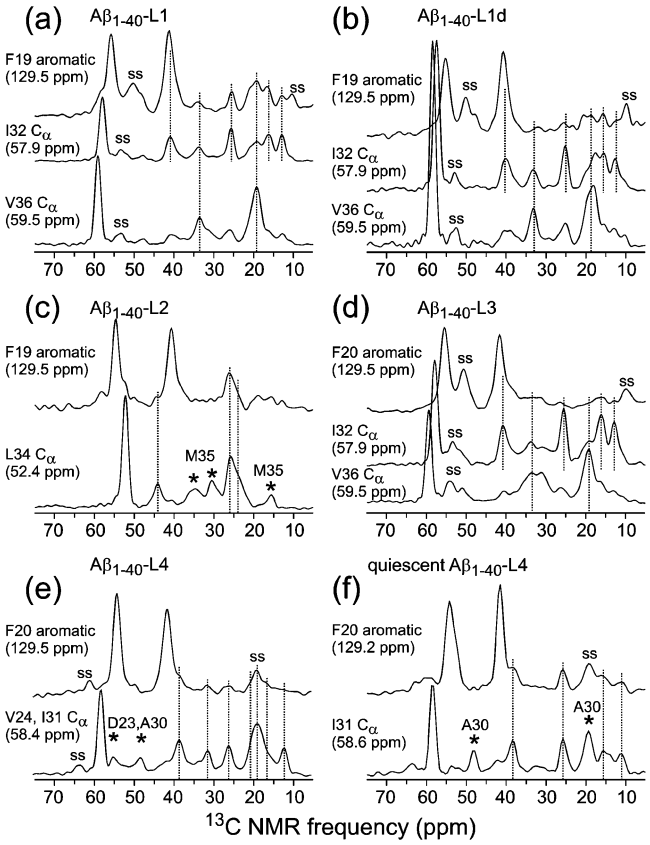

FIGURE 3: 1D slices of 2D solid-state ^{13}C-^{13}C NMR spectra of the indicated Aβ_{1-40} fibril samples, taken at the indicated ^{13}C NMR chemical shifts. Alignment of peaks in F19 or F20 aromatic slices with peaks in the C_α slices of other ^{13}C-labeled residues allows the identification of aliphatic/aromatic cross-peaks that indicate quaternary contacts. Panels (a) and (c) show the presence of F19/I32, F19/V36, and F19/L34 contacts. Panels (d) and (e) show the absence of F20/I32, F20/V36, and F20/I31 contacts. Panel (b) demonstrates the effect of isotopic dilution on F19/I32 and F19/V36 contacts. Panel (f) shows the presence of F20/I31 contacts in fibrils grown under quiescent conditions. Measurement conditions as in Figure 2, with MAS frequencies of 18.00 kHz in (a), (b), and (d), 21.50 kHz in (c), and 16.60 kHz in (e) and (f). Peaks arising from MAS sidebands are indicated by "ss". Asterisks indicate peaks from the indicated residues, due either to partial overlap of ^{13}C NMR lines or to cross-peaks between signals of sequential ^{13}C-labeled residues.

selective rotational echo double resonance (REDOR) technique (*67*, *68*). These measurements were carried out at 9.39 and 14.1 T fields with a 9.00 kHz MAS frequency, 10−15 μs hard ^{15}N π pulse lengths, and frequency-selective Gaussian π pulse lengths (at the NMR frequencies of side chain amine ^{15}N and carboxylate ^{13}C sites) of approximately 1 ms. Each REDOR build-up curve in Figure 4a was obtained in approximately 170 h with a 2 s recycle delay.

Quaternary contacts between side chain methyl ^{13}C and backbone amide ^{15}N sites were detected with the 2D transferred echo double resonance (TEDOR) technique of Jaroniec et al. (*69*−*71*). These measurements were carried out at 14.1 T with an 11.14 kHz MAS frequency and 50 kHz rf fields for all ^{13}C and ^{15}N pulses. No frequency-selective pulses were used. 2D ^{15}N-^{13}C spectra were obtained in 100−174 h with a 2 s recycle delay.

^{13}C NMR chemical shift assignments were obtained previously from 2D ^{13}C-^{13}C NMR spectra. A table of ^{13}C NMR chemical shift assignments is available as on-line Supporting Information for ref *11*. ^{15}N NMR chemical shift assignments were obtained from 2D ^{15}N-^{13}C NMR as in Figure 6a. ^{13}C NMR chemical shifts are relative to tetramethylsilane, based on an external adamantane reference at 38.56 ppm. ^{15}N NMR chemical shifts are relative to liquid NH_3, based on the published ratios of ^{13}C and ^{15}N NMR frequencies (*72*).

Generation of Structural Models. Structural models depicted in Figures 1, 7, and 8 were generated with the MOLMOL (*73*) and TINKER/Force Field Explorer (available at http://dasher.wustl.edu/tinker/) programs. The charmm27 force field was used in molecular dynamics (MD) and energy minimization runs in TINKER, with all electrostatic terms switched off. Restraints on certain interatomic distances and backbone torsion angles were enforced by harmonic potential energy functions, as described below.

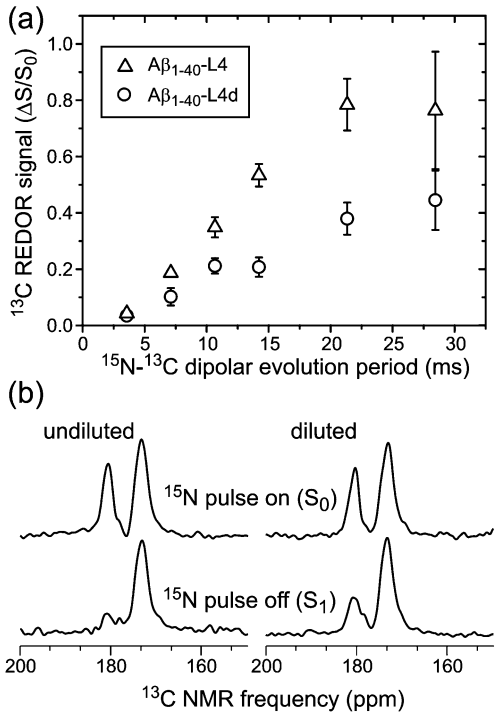

FIGURE 4: (a) Frequency-selective ^{15}N-^{13}C REDOR data for Aβ_{1-40}-L4 (triangles) and Aβ_{1-40}-L4d (circles) fibrils, recorded at 14.1 T with a 9.00 kHz MAS frequency and with selective refocusing pulses near the NMR frequencies of D23 C_γ and K28 N_ζ. The build-up of the normalized REDOR difference signal $\Delta S/S_0$ for D23 C_γ in Aβ_{1-40}-L4 fibrils with increasing evolution period indicates an interatomic distance of roughly 3.7 Å between D23 C_γ and K28 N_ζ. The lower asymptotic value of $\Delta S/S_0$ for Aβ_{1-40}-L4d fibrils indicates that close contacts between D23 C_γ and K28 N_ζ sites are primarily intermolecular. (b) S_0 and S_1 spectra from frequency-selective REDOR measurements at a 21.33 ms evolution period, obtained at 9.39 T, demonstrating the frequency selectivity and the effect of isotopic dilution. NMR lines at 180.8 and 173 ppm are from D23 C_γ and backbone carbonyl sites, respectively. S_0 and S_1 measurements differ only by a single selective ^{15}N refocusing pulse, and $\Delta S \equiv S_0 - S_1$.

For each model in Figure 1b, an initial Aβ_{9-40} conformation was constructed in MOLMOL with backbone torsion angles $\phi = -140°$ and $\psi = 138°$ for residues 9−24 and 31−40, and with backbone torsion angles chosen manually for residues 25−30 to produce approximately the desired internal quaternary contacts while allowing for a salt bridge interaction between D23 and K28 side chains. Three copies of the initial Aβ_{9-40} conformation were combined, with 4.8 Å displacements along the direction of intermolecular hydrogen bonds for the β-strand segments. Restrained energy minimization of the trimeric structure was then carried out. Backbone torsion angles of residues 16−23 and 30−39 were restrained to $\phi = -140°$ and $\psi = 140°$. Intermolecular hydrogen bonds for residues 10−24 and 30−39 in in-register, parallel β-sheets were enforced by 2.15 Å distance restraints between backbone carbonyl oxygen and amide hydrogen atoms. Intramolecular distances between D23 C_γ and K28 N_ζ were restrained to the 3.5−4.5 Å range. Intramolecular distances between C_α of E22 and C_α of G33 and between C_α of V18 and C_α of G37 were restrained to the 8.0−10.0 Å range. Force constants were 0.01 kcal/mol-deg^2 for backbone torsion angles and 10.0 kcal/mol-Å^2 for interatomic distances. Restraints for the four models in Figure 1b differed only in the choice of backbone hydrogen bond directions for the N-terminal and C-terminal β-strands. Models displayed in Figure 1b are the central molecules in energy-minimized trimeric structures. Models in Figure 1a were constructed manually in MOLMOL from multiple copies of the F19/L34 model in Figure 1b.

For models in Figure 7, six copies of the F19/L34 model in Figure 1b were first combined with 4.8 Å displacements along the direction of intermolecular hydrogen bonds. Restrained energy minimization of the hexameric structure was then carried out, followed by a 10−100 ps restrained MD simulation at 400 K and a final restrained energy minimization. Restraints included the backbone torsion angle and intermolecular hydrogen bond distance restraints described above, in addition to 4.0−6.0 Å distance restraints between F19 C_ζ and I32 C_δ, between F19 C_ζ and L34 C_δ, and between F19 C_ζ and V36 C_γ, and 3.5−4.5 Å distance restraints between D23 C_γ and K28 N_ζ. These side chain distance restraints were intermolecular, connecting D23 and F19 of molecule i with K28, I32, L34, and V36 of molecule i + 1, i − 1, i + 2, or i − 2 to produce the STAG(+1), STAG(−1), STAG(+2), and STAG(−2) models.

For models in Figure 8, 12 copies of the F19/L34 model in Figure 1b were first positioned manually in MOLMOL to approximate a C_{2z} structure with the internal and external quaternary contacts indicated by solid-state NMR data in Figures 2−6. Several rounds of restrained energy minimization and restrained MD at 500 K were then performed until STAG(+2) or STAG(−2) stagger was achieved, using a temporary restraint set that included backbone torsion angle restraints for residues 10−12, 15−21, 30−32, 34−36, and 39 ($\phi = -150°$, $\psi = 150°$, 0.01 kcal/mol-deg^2 force constants), backbone hydrogen bond distance restraints for residues 10−24 and 30−40 (2.15 Å oxygen−hydrogen distances, 10.0 kcal/mol-Å^2 force constants), intermolecular distance restraints between F19 C_ζ and I32 C_δ, F19 C_ζ and L34 C_δ, and F19 C_ζ and V36 C_γ (2.0−8.0 Å ranges, 1.0 kcal/mol-Å^2 force constants), between M35 C_ϵ and G33 N (2.0−4.0 Å range, 0.1 kcal/mol-Å^2 force constant), between I31 C_δ and G37 C_α (2.0−8.0 Å range, 0.1 kcal/mol-Å^2 force constant), between D23 C_γ and K28 N_ζ (3.0−4.5 Å distance, 10.0 kcal/mol-Å^2 force constant), and between V12 C_α and V40 C_γ, L17 C_γ and M35 C_α, and Q15 C_δ and G37 C_α (3.0 Å, 10.0 kcal/mol-Å^2 force constants), and intramolecular distance restraints between M35 C_ϵ and G37 C_α (2.0−6.0 Å, 0.1 kcal/mol-Å^2 force constant). In this temporary restraint set, F19/I32, F19/L34, F19/V36, D23/K28, V12/V40, L17/M35, and Q15/G37 distance restraints were between peptide molecule i and molecule i + 2 or i − 2 within a single molecular layer (representing internal quaternary contacts) to produce the models in Figure 8, panel a or b. M35/G33 and I31/G37 distance restraints were between molecules in different molecular layers (representing external quaternary contacts).

Once the desired stagger of internal quaternary contacts was achieved, the restraint set was changed to its final form by eliminating the V12/V40, L17/M35, and Q15/G37 distance restraints, reducing the force constants for F19/I32, F19/L34, and F19/V36 distance restraints to 0.1 kcal/mol-Å^2, and adding intermolecular distance restraints between L17 C_δ and I32 C_δ (2.0−8.0 Å range, 0.1 kcal/mol-Å^2 force constant). In the final restraint set, F19/I32, F19/L34, F19/V36, D23/K28, and L17/I32 side chain distance restraints

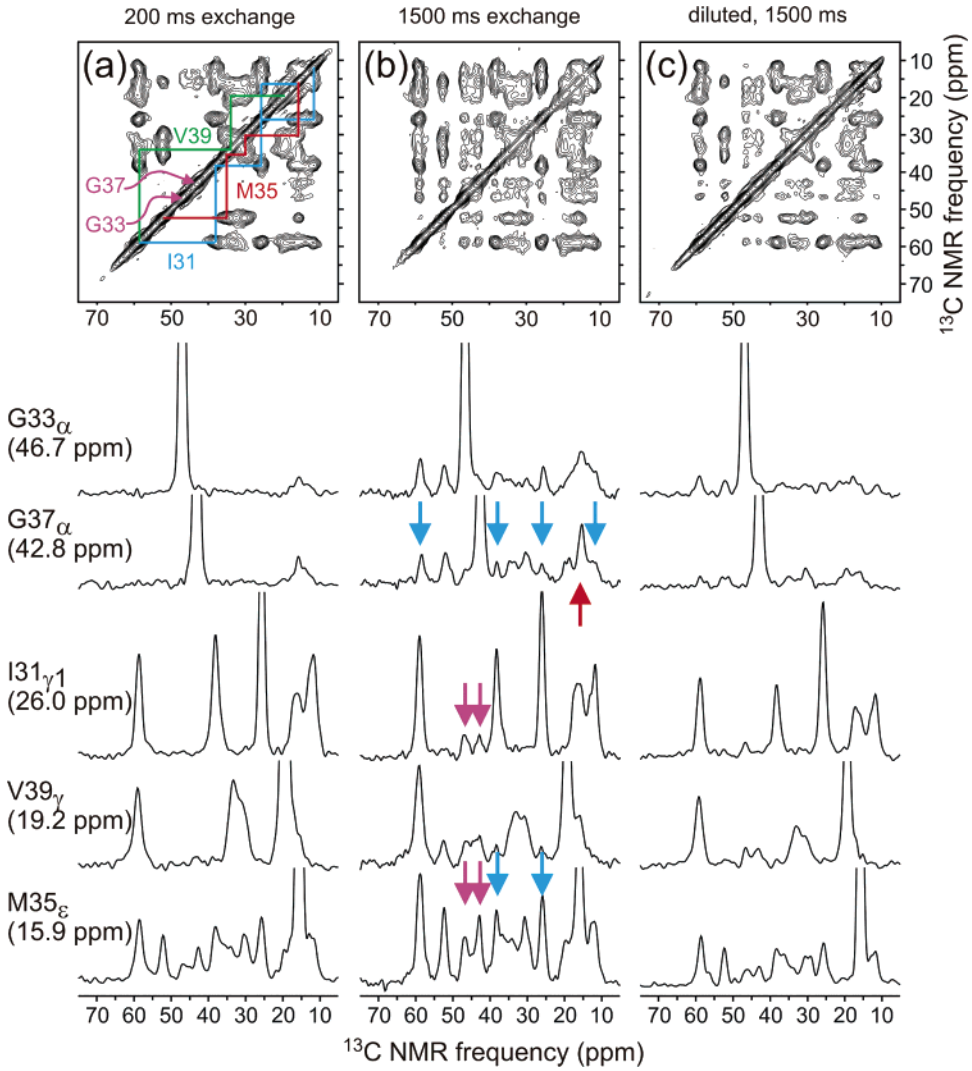

FIGURE 5: 2D solid-state ^{13}C-^{13}C NMR spectra of Aβ_{1-40}-L5 (a, b) and Aβ_{1-40}-L5d (c) fibrils, recorded at 14.1 T with a 23.50 kHz MAS frequency and indicated mixing periods. Resonance assignment pathways are shown in panel (a). 1D slices at indicated NMR frequencies are shown beneath each 2D spectrum. Blue arrows indicate I31/G37 and I31/M35 interresidue cross-peaks. Purple arrows indicate M35/G33 and M35/G37 cross-peaks. Red arrow indicates a G37/M35 cross-peak. Vertical scales are identical in all 1D slices in the same column.

were between molecule i and molecules i + 1 and i + 2 or between molecule i and molecules i − 1 and i − 2 within a single molecular layer. Ten rounds of alternating restrained energy minimizations and restrained MD simulations at 500 K for 5 ps were performed with the final restraints (all of which are based on experimental data) to generate a bundle of structural models. The high-temperature MD simulations produced significant conformational rearrangements between energy minimizations, so that the final bundle of structural models depicts the extent to which the Aβ_{1-40} fibril structure is determined by the experimentally based restraints.

We emphasize that certain structural details in the models in Figure 8 (e.g., backbone and side chain torsion angles) are not determined uniquely or precisely by the experimental data. This point is discussed in greater detail below.

RESULTS

Constraints on Internal Quaternary Contacts. Figure 2 shows a 2D ^{13}C-^{13}C NMR spectrum of Aβ_{1-40}-L1 fibrils, obtained with a 500 ms mixing period between the two spectroscopic dimensions. Under the conditions of this measurement, cross-peaks are detected that connect ^{13}C NMR chemical shifts of ^{13}C-labeled sites in nonsequential residues. In contrast, only intraresidue cross-peaks are detected in analogous spectra with mixing periods less than 50 ms (data not shown). Of particular interest are cross-peaks between the aromatic ^{13}C NMR lines of F19 and aliphatic ^{13}C NMR lines of I32 and V36, which indicate interatomic distances of approximately 6 Å or less (see below) between the F19 side chain and the I32 and V36 side chains. Given the secondary structure of Aβ_{1-40} fibrils depicted in Figure 1, we interpret the observed F19/I32 and F19/V36 cross-peaks as support for internal quaternary contacts resembling those in the F19/L34 model in Figure 1b.

Figure 3 shows 1D slices through 2D ^{13}C-^{13}C NMR spectra of several samples with different sets of labeled residues (see Table 1 for sample definitions), all obtained with 500 ms mixing periods. Slices are taken at ^{13}C NMR chemical shifts of the maximum aromatic signal intensity and of the C$_\alpha$ NMR lines of I31, I32, L34, or V36. The C$_\alpha$ slices allow the chemical shifts of the relevant aliphatic side chain sites to be identified (vertical lines in Figure 3), due to nearly

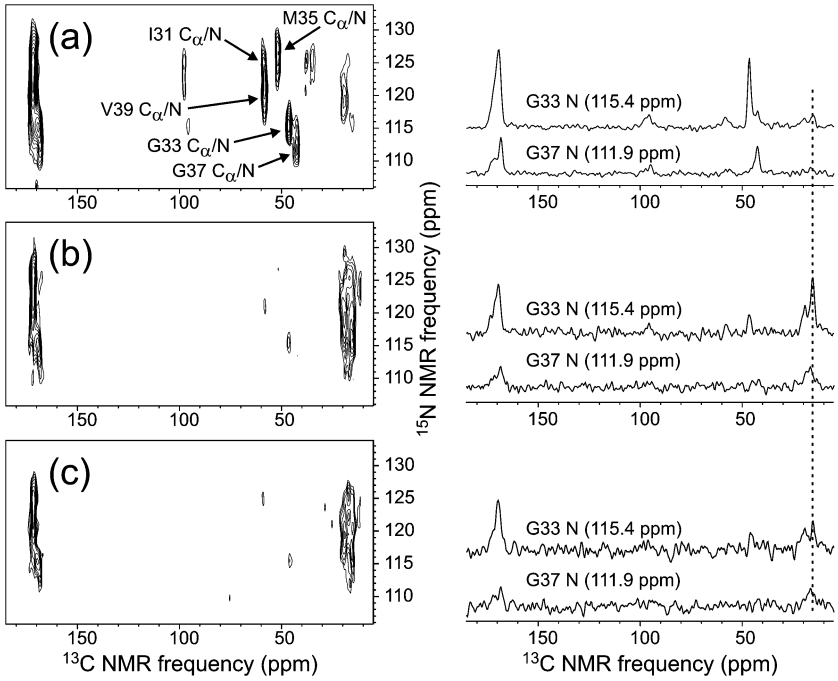

FIGURE 6: 2D solid-state ^{15}N-^{13}C NMR spectra of Aβ_{1-40}-L5 (a, b) and Aβ_{1-40}-L5d (c) fibrils, recorded at 14.T with a 11.14 kHz MAS frequency and TEDOR recoupling periods of 2.873 ms (a) or 5.745 (b, c). Assignments of one-bond $^{13}C_\alpha/^{15}$N cross-peaks are shown in panel (a). 1D slices at the indicated ^{15}N NMR frequencies are shown to the right of each 2D spectrum. Dashed line indicates the ^{13}C NMR chemical shift of M35 C_ϵ.

complete redistribution of ^{13}C nuclear spin polarizations within each side chain during the mixing period. The aromatic slices show interresidue cross-peaks to certain aliphatic side chain sites, in addition to stronger intraresidue cross-peaks to C_α and C_β sites of F19 or F20. In Aβ_{1-40}-L1 fibrils (Figure 3a), cross-peaks from F19 to C_γ1, C_γ2, and C_δ sites of I32 (25.4, 16.1, and 12.6 ppm) and to C_β and C_γ sites of V36 (33.1 and 19.0 ppm) are observed unambiguously. In Aβ_{1-40}-L2 fibrils (Figure 3c), cross-peaks from F19 to C_γ and C_δ of L34 (broad peak at 25 ppm) are observed. In Aβ_{1-40}-L3 fibrils (Figure 3d), cross-peaks from F20 to I32 and V36 are not observed, showing that the aromatic/aliphatic cross-peaks are structurally specific under these measurement conditions. These data support the F19/L34 model in Figure 1b.

Figure 3e,f provides further evidence for the structural specificity of the 2D ^{13}C-^{13}C NMR measurements and for the existence of molecular-level structural polymorphism in Aβ_{1-40} fibrils (*11*). Aβ_{1-40}-L4 fibrils grown from quiescent fibril seeds show strong F20/I31 cross-peaks (Figure 3f). F20/I31 cross-peaks are much weaker or absent in the spectrum of Aβ_{1-40}-L4 fibrils grown from agitated fibril seeds (Figure 3e). Strong F20/I31 cross-peaks in agitated fibrils would be inconsistent with the F19/L34 model in Figure 1b. Agitated and quiescent Aβ_{1-40} fibrils apparently differ in their internal quaternary contacts, in addition to other structural characteristics such as protofilament MPL (*11*).

In addition to the aromatic/aliphatic contacts identified in Figure 3, an L17/I32 aliphatic/aliphatic contact was observed in an analogous spectrum of agitated Aβ_{1-40} fibrils with uniformly ^{15}N,^{13}C-labeled S8, H13, L17, V18, A21, I32, and G33 (data not shown).

Interpretation of interresidue cross-peak intensities in spectra such as those in Figures 2 and 3 in terms of precise distances between specific pairs of ^{13}C-labeled sites is not possible because these cross-peak intensities are determined by a network of magnetic dipole−dipole couplings, both intraresidue and interresidue, among many ^{13}C nuclei with unknown geometry. Couplings to ^{1}H nuclei also play a large role, making accurate numerical simulations for any given geometry intractable. To obtain an empirical estimate of the distance range probed by our 2D ^{13}C-^{13}C NMR measurements, we have measured the extent of nuclear spin polarization transfer from aromatic ^{13}C sites to aliphatic ^{13}C sites in a sample of polycrystalline Phe-Val, a dipeptide with known crystal structure (*74*). In this sample, molecules with uniformly ^{15}N,^{13}C-labeled phenylalanine were cocrystallized with molecules with uniformly ^{15}N,^{13}C-labeled valine, in a 1:5 molar ratio. Experimental conditions were essentially the same as in Figures 2 and 3. After mixing periods of 100, 200, and 500 ms, nuclear spin polarizations of valine aliphatic sites were 4.4 ± 0.4%, 8.8 ± 0.4%, and 19 ± 2% of the nuclear spin polarizations of phenylalanine aromatic sites, as determined from ^{13}C NMR signal intensities. Fitting these data to an exponential form, we extract a characteristic time $\tau = 2300$ ms for intermolecular aromatic-to-aliphatic polarization transfer in Phe-Val. The shortest intermolecular distances between aromatic and aliphatic carbons in Phe-Val are 3.9 Å (*74*). If $\tau \propto R^6$, as might be expected for incoherent polarization transfer between isolated pairs of dipole-coupled ^{13}C nuclei with internuclear distance R, if $R = 3.9$ Å for Phe-Val, and if a 10% polarization transfer were detectable, then the maximum detectable distance would be $R_{max} \approx 4.4$ Å. If $\tau \propto R^2$, as might be expected if polarization transfer were a diffusive process, then $R_{max} \approx 5.6$ Å. On the basis of these results, we estimate that the interresidue cross-peaks discussed above indicate interatomic distances up to approximately 6 Å. Note that this distance estimate applies to the shortest distance between ^{13}C-labeled sites of the two residues in question. Distance limits of 8 Å are used in the

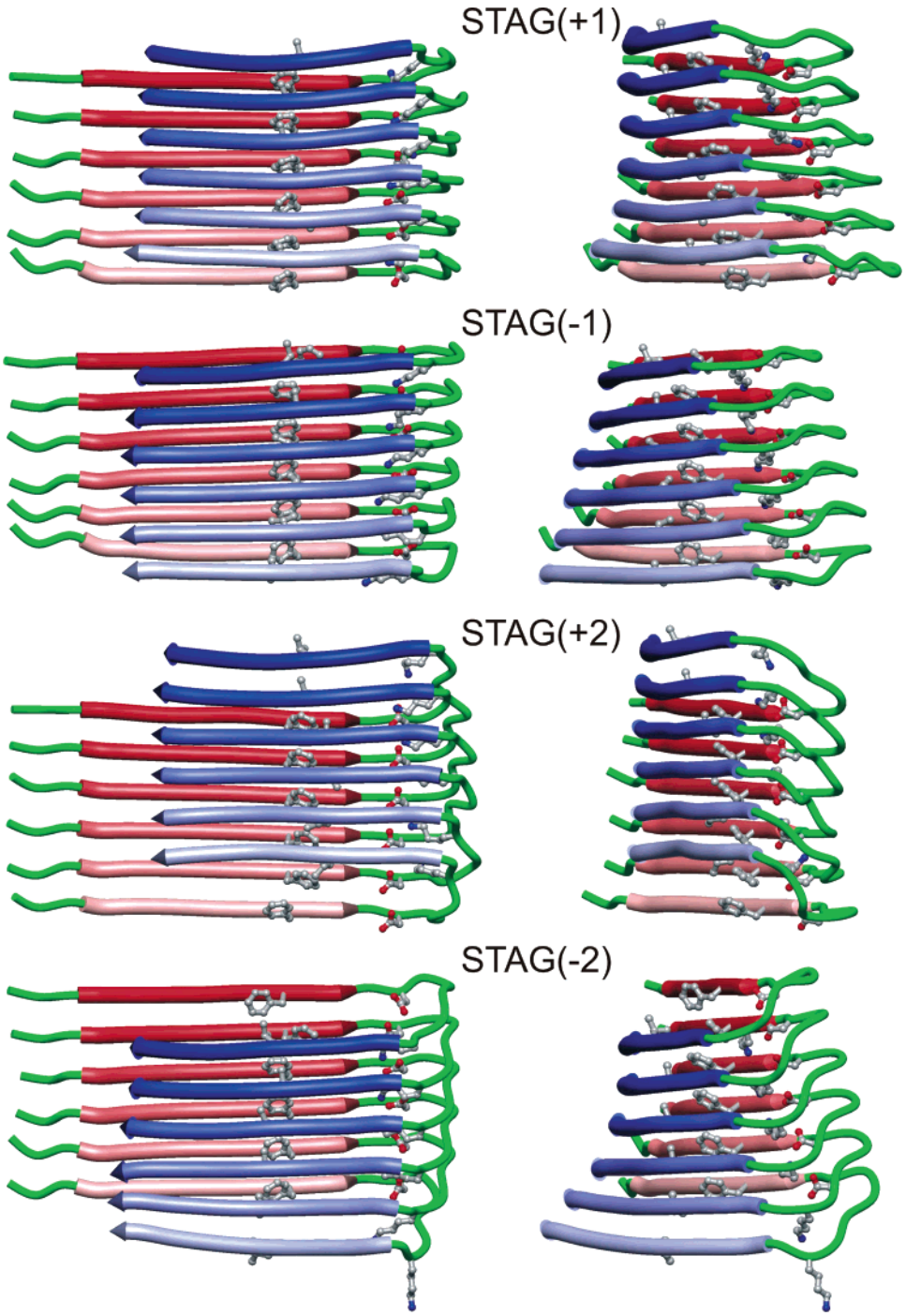

FIGURE 7: Four candidate models for the internal quaternary contacts within Aβ_{1-40} fibrils, with different degrees and directions of stagger. Side chains of F19, D23, K28, and L34 are shown. Representations on the right are rotated by 60° about the *z* axis relative to those on the left.

modeling calculations (see Materials and Methods) due to the unknown identities of the closest sites. These distance limits are consistent with the interpretation of interresidue ^{13}C-^{13}C cross-peaks in similar measurements on microcrystalline proteins of known structure (*75*).

Shortest intramolecular distances between side chain carbon nuclei of F19 and side chain carbon nuclei of I32, L34, and V36 are 3.8 Å, 3.9 Å, and 7.8 Å for the F19/L34 model in Figure 1b, 15.3 Å, 10.1 Å, and 8.0 Å for the F20/L34 model, 7.0 Å, 7.8 Å, and 12.4 Å for the F19/M35 model, and 18.3 Å, 15.5 Å, and 15.2 Å for the F20/M35 model. These are distances in models generated without inclusion of F19/I32, F19/L34, or F19/V36 distance restraints, but they strongly suggest that only the F19/L34 model has quaternary contacts consistent with data in Figures 2 and 3.

D23/K28 Salt Bridge Interaction. Figure 4a shows ^{13}C-detected frequency-selective REDOR data for Aβ_{1-40}-L4. In these measurements, frequency-selective rf pulses permit detection of the ^{15}N-^{13}C magnetic dipole−dipole coupling between C_γ of D23 and N_ζ of K28, despite the presence of multiple ^{15}N- and ^{13}C-labeled sites in Aβ_{1-40}-L4 (*68*). For isolated ^{15}N-^{13}C pairs with internuclear distance R_{NC}, one expects a build-up of the REDOR $\Delta S/S_0$ signal with increasing evolution period τ_{REDOR} such that $\Delta S/S_0$ reaches

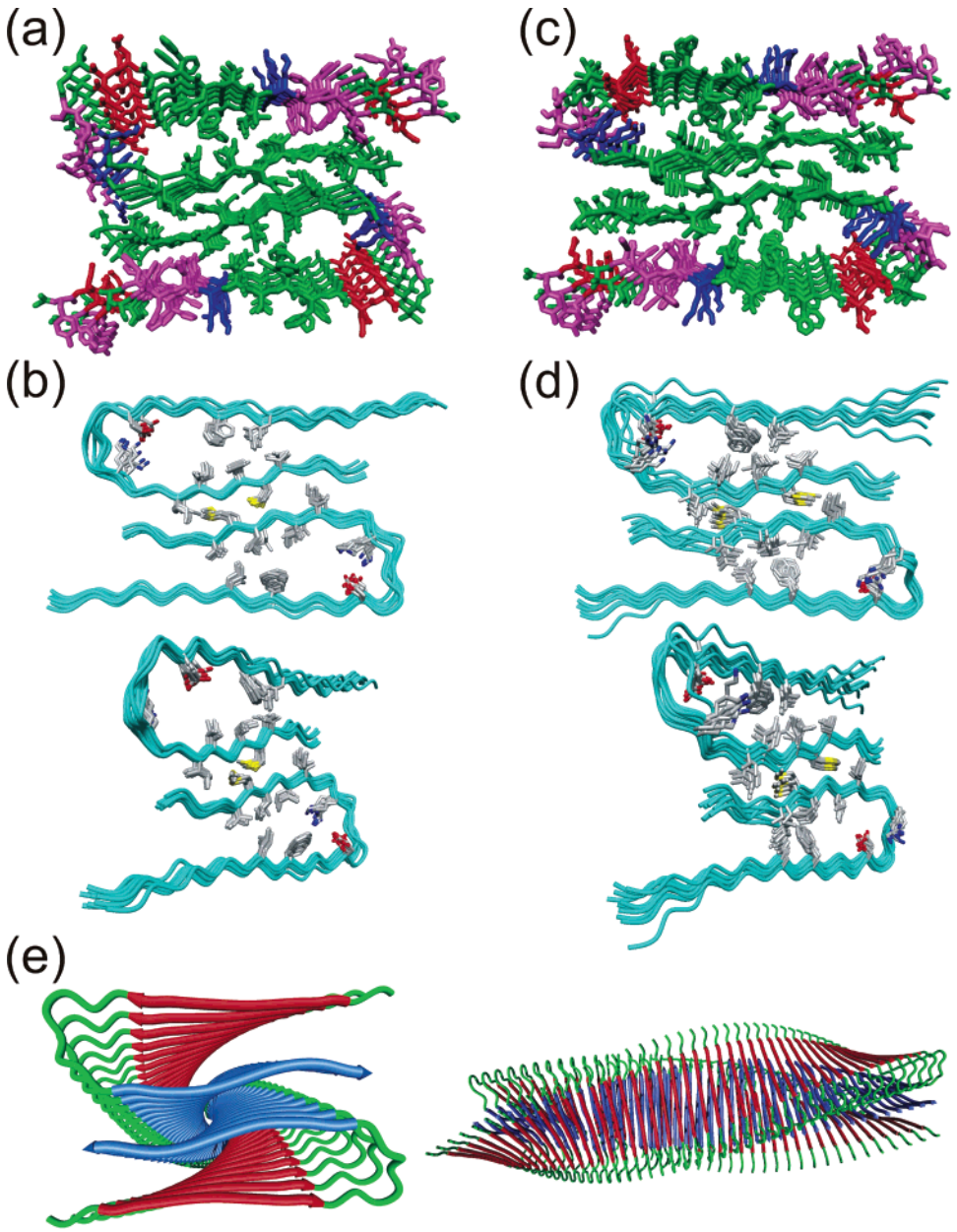

FIGURE 8: Structural models for Aβ_{1-40} fibrils with F19/L34 internal quaternary contacts, C_{2z} symmetry, and either STAG(+2) stagger (a, b, e) or STAG(−2) stagger (c, d). Models were generated by a restrained molecular dynamics and restrained energy minimization protocol, applied to a dodecameric cluster of Aβ_{9-40} molecules, with all restraints being derived from solid-state NMR measurements. Residues 1−8 are disordered, and were omitted from the modeling calculations. Panels (a) and (c) show averages of 10 energy-minimized structures, as calculated by MOLMOL (*73*). Hydrophobic (G, A, F, V, L, I, M), negatively charged (D, E), positively charged (K), and polar (Y, H, Q, N, S) residues are colored green, red, blue, and magenta, respectively. Panels (b) and (d) show bundles of central pairs of molecules in 10 energy-minimized structures. Side chains of L17, F19, D23, K28, I31, I32, L34, M35, and V36 are shown. Upper view is along the *z* axis. Lower view is rotated by 45° about the *y* axis. Panel (e) shows a cartoon representation of a full fibril, viewed parallel and perpendicular to *z*, generated from multiple copies of a central pair of molecules in panel (a), with 4.8 Å displacements along *z* and an arbitrarily chosen twist of 0.833°/Å. Atomic coordinates for panels (a−d) are available upon request (e-mail address: robertty@mail.nih.gov).

half its maximum value at $\tau_{REDOR} = 0.257$ ms × (R_{NC}^3/Å^3) (*41*, *67*, *68*). If each ^{13}C nucleus is coupled to more than one ^{15}N nucleus, the REDOR build-up curve is dominated by the shortest ^{15}N-^{13}C distance. Therefore, the data for Aβ_{1-40}-L4 in Figure 4a, in which the half-maximum occurs at 12.5 ± 1.5 ms, indicate nearest-neighbor ^{15}N-^{13}C distances of approximately 3.7 Å, consistent with salt bridge interactions between the side chains of D23 and K28.

The spectra in Figure 4b demonstrate the selectivity of our frequency-selective REDOR data. The intensities of D23 $^{13}C_\gamma$ NMR lines (at 180.8 ppm) differ significantly in S_0 and S_1 spectra. The intensities of the backbone ^{13}CO signals (at 173 ppm) are the same in S_0 and S_1 spectra, despite the fact that every backbone ^{13}CO label is within approximately 2.4 Å of a backbone amide ^{15}N label.

As shown previously (*10*), NMR chemical shifts indicate that the D23 and K28 side chains are ionized in Aβ_{1-40} fibrils. Frequency-selective REDOR measurements have shown the absence or partial population of D23/K28 salt bridge interactions in fibrils grown under quiescent conditions (*11*).

Constraints on External Quaternary Contacts. Figure 5 shows 2D ^{13}C-^{13}C NMR spectra of Aβ_{1-40}-L5 fibrils. With a 1500 ms mixing period, but not a 200 ms period, cross-

peaks between the $^{13}C_\alpha$ NMR line of G37 and aliphatic ^{13}C NMR lines of I31 are observed unambiguously (blue arrows in G37α slice, Figure 5b). Given that I31 and G37 reside in a single β-strand, the intramolecular distances between G37 C_α and I31 aliphatic sites are approximately 20 Å, too large to produce the observed cross-peaks. We therefore attribute the G37/I31 cross-peaks to external quaternary contacts, favoring the C_{2z} model over the C_{2x} model in Figure 1a. The fact that cross-peaks between the $^{13}C_\alpha$ NMR line of G37 and the $^{13}C_\epsilon$ NMR line of M35 are more intense than the corresponding G33/M35 cross-peaks (red arrow in G37α slice and purple arrows in M35ϵ slice, Figure 5b) suggests that the M35 side chain tilts toward G37 rather than G33, as depicted in the F19/L34 model in Figure 1b.

Additional constraints on external quaternary contacts in Aβ_{1-40} fibrils come from the 2D ^{15}N-^{13}C NMR spectrum in Figure 6. The spectrum in Figure 6a, obtained with 2.87 ms ^{15}N-^{13}C TEDOR evolution periods, shows strong intraresidue $^{13}C_\alpha$/^{15}N cross-peaks that permit site-specific assignment of backbone amide ^{15}N chemical shifts for labeled residues in Aβ_{1-40}-L5 fibrils. With 5.75 ms TEDOR periods (Figure 6b), cross-peaks between side chain methyl ^{13}C NMR lines and backbone amide ^{15}N NMR lines become more intense, while $^{13}C_\alpha$/^{15}N cross-peaks are attenuated by the relatively rapid transverse spin relaxation of $^{13}C_\alpha$. A strong cross-peak between the $^{13}C_\epsilon$ NMR line of M35 and the ^{15}N line of G33 is observed, while the corresponding M35/G37 cross-peak is absent. We attribute the M35/G33 cross-peak to an external contact between the M35 side chain and the peptide backbone at G33. The fact that the volume of the cross-peak between $^{13}C_\epsilon$ of M35 and ^{15}N of G33 is about equal to the volumes of intraresidue ^{13}CO/^{15}N cross-peaks suggests that the intermolecular distance between C_ϵ of M35 and N of G33 is roughly 3 Å.

Figure 6c shows that the M35/G33 cross-peak intensity is reduced by a factor of 2 or more (relative to the intraresidue ^{13}CO/^{15}N cross-peak of G33) when Aβ_{1-40}-L5 is diluted to 33% in unlabeled Aβ_{1-40}, producing the Aβ_{1-40}-L5d fibril sample. This result indicates that the approximate 3 Å distance between C_ϵ M35 and N of G33 is an intermolecular distance, consistent with our interpretation of the M35/G33 cross-peak as evidence for an external quaternary contact.

C_{2z} symmetry is also favored over C_{2x} symmetry by the observation of a single set of ^{13}C NMR chemical shifts for side chain sites in Aβ_{1-40}-L5 fibrils. Interdigitation of side chains at the external interface would necessarily lower the symmetry of a C_{2x} structure (*76*), shifting the two molecular layers relative to one another and placing the I31, M35, and V39 side chains of the two layers in qualitatively different structural environments. One would then expect to observe splittings of the ^{13}C NMR lines due to structural inequivalence of the two molecular layers at the external quaternary contacts. No splittings are observed in Figure 4 or in any other spectra of Aβ_{1-40}-L5 fibrils.

In all-atom representations of the models in Figure 1a, the shortest distance between side chain nuclei of I31 and C_α of G37 is 5.2 Å for C_{2z} symmetry and 19.1 Å for C_{2x} symmetry. Both symmetries lead to 4.6 Å distances between C_ϵ of M35 and N of G33 in different molecular layers, but only half of the C_ϵ nuclei participate in a 4.6 Å distance with C_{2x} symmetry. The shortest distance is 16.4 Å for the remaining C_ϵ nuclei. These are distances in models generated without inclusion of distance restraints based on the data in Figures 2, 3, 5, and 6, but they strongly suggest that C_{2z} symmetry is consistent with the experimental data, while C_{2x} symmetry is not.

Staggering of Internal Quaternary Contacts. When a single peptide molecule contributes β-strand segments to more than one β-sheet in an amyloid fibril, the displacement of the β-sheets along the direction of the long fibril axis becomes an additional structural variable that we refer to as "stagger". Figure 7 shows idealized models for a single molecular layer in Aβ_{1-40} fibrils with four distinct staggers. In the STAG(+1) and STAG(−1) models, the C-terminal β-strand of each molecule is displaced by approximately 2.4 Å (i.e., half the interstrand spacing in one β-sheet) relative to the N-terminal β-strand of the same molecule. Note that the two ends of a cross-β unit constructed from in-register, parallel β-sheets are inequivalent, with backbone amide N−H bonds of even-numbered residues and odd-numbered residues in the same β-sheet pointing toward opposite ends. Therefore, STAG(+1) and STAG(−1) models are structurally distinct. In the STAG(+2) and STAG(−2) models, the C-terminal β-strand of each molecule is displaced by approximately 7.2 Å (i.e., 1.5 times the interstrand spacing) relative to the N-terminal β-strand of the same molecule. Displacements by odd multiples of half the interstrand spacing are expected to optimized the packing of side chains at interfaces between β-sheets. The size of the displacement is obviously limited by the length of the loops between β-strand segments.

STAG(±1) and STAG(±2) models differ as to whether internal quaternary contacts (e.g., the F19/I32 and F19/V36 contacts indicated by the data in Figures 2 and 3a) are both intramolecular and intermolecular (for STAG(±1) models) or purely intermolecular (for STAG(±2) models). In principle, comparisons of solid-state NMR data from fibrils in which all peptide molecules are isotopically labeled with data from fibrils in which only a fraction of the molecules are labeled permits intramolecular contacts to be distinguished intermolecular contacts. Figures 3 and 4 show the results of such isotopic dilution experiments. Dilution of Aβ_{1-40}-L1 in unlabeled Aβ_{1-40}, producing the Aβ_{1-40}-L1d sample, results in a reduction of F19/I32 cross-peak intensities relative to intraresidue F19 cross-peak intensities by a factor of 0.50 ± 0.15 (Figure 3a,b). F19/V36 cross-peak intensities are reduced by a factor of 0.40 ± 0.20. Assuming that F19/I32 or F19/V36 cross-peak intensities (normalized to intraresidue cross-peak intensities) are proportional to the average number of quaternary contacts of a labeled F19 side chain to labeled side chains of I32 or V36, one expects a reduction of intraresidue cross-peak intensity by a factor of 0.65 for 31% labeling in STAG(±1) structures (factor of $(1 + x)/2$ for labeled fraction x) and a factor of 0.31 for 31% labeling in STAG(±2) structures (factor of x). In Figure 4a, dilution of Aβ_{1-40}-L4 in unlabeled Aβ_{1-40}, producing the Aβ_{1-40}-L4d sample, results in a reduction of the $\Delta S/S_0$ values in frequency-selective REDOR data by a factor of 0.50 ± 0.07. Assuming that each D23 side chain interacts with two K28 side chains (due to interdigitation of the oppositely charged side chains (*76*)) and that the $\Delta S/S_0$ value is proportional to the probability that a labeled D23 side chain interacts with at least one labeled K28 side chain, one expects no reduction of $\Delta S/S_0$ in STAG(±1) structures and a reduction by 0.44 for 33% labeling in STAG(±2) structures (factor of (1 −

$x)^2$). Thus, the combined data for Aβ_{1-40}-L1d and Aβ_{1-40}-L4d fibril samples favor STAG(±2) models.

DISCUSSION

Explicit Structural Models for Aβ_{1-40} Fibrils. Figure 8 shows explicit models for the molecular structure of Aβ_{1-40} fibrils, constructed with the high-temperature MD/energy minimization protocol described above (see Materials and Methods). Because our data do not distinguish STAG(+2) from STAG(−2) structures, models with both staggers are shown. Residues 1−8 are omitted, as these residues are known to be structurally disordered from solid-state NMR line width data (*10*, *11*), measurements of intermolecular ^{13}C-^{13}C dipole−dipole couplings (*37*, *38*), hydrogen exchange data (*26*, *27*), and proteolysis data (*61*, *62*). All structural restraints used in the final MD/energy minimization protocol were based on experimental measurements, including previously reported NMR chemical shift data (*11*) and intermolecular distance measurements (*37*, *38*) in addition to the data in Figures 2−6. Atomic coordinates are available upon request (e-mail address: robertty@mail.nih.gov).

The STAG(+2) (Figure 8a,b,e) and STAG(−2) (Figure 8c,d) models are quite similar. In both models, side chains of L17, F19, I32, L34, and V36 create a hydrophobic cluster that apparently stabilizes the fold of a single molecular layer (i.e., the internal quaternary contacts). Glycines at residues 33, 37, and 38 create grooves into which the side chains of I31 and M35 fit at the interface between molecular layers (i.e., the external quaternary contacts). Oppositely charged D23 and K28 side chains interact in an intermolecular fashion but in the interior of a single molecular layer with STAG(±2) stagger. Models in Figure 8 contain channels that are lined by side chains of F19, A21, D23, K28, A30, and I32. These channels may contain "water wires", as suggested by recent MD simulations in explicit solvent (*76*). We find that the ^{13}C NMR line widths for D23 and K28 side chain sites are reduced significantly in hydrated Aβ_{1-40} fibrils compared with those in lyophilized Aβ_{1-40} fibrils (e.g., 2.0, 1.5, and 1.2 ppm for C_γ, C_δ, and C_ϵ of K28 in the hydrated state, compared with >2.5 ppm in the lyophilized state), possibly due to motional narrowing associated with mobile water molecules in these channels. Other charged and polar side chains are outside the hydrophobic core of the models in Figure 8.

Aβ_{1-40} molecules with oxidized M35 side chains have been shown to be resistant to fibril formation, relative to unoxidized Aβ_{1-40} (*77*, *78*). Oxidation greatly increases the polarity of the M35 side chain (*79*), possibly destabilizing the external quaternary contacts and thereby inhibiting fibril formation.

Models in Figure 8 represent the Aβ_{1-40} protofilament, i.e., the minimal structural unit in Aβ_{1-40} fibrils. In EM images of agitated Aβ_{1-40} fibrils, the protofilaments have widths of 50 ± 5 Å and typically associate in a parallel manner, forming flat bundles of 2−5 protofilaments (*11*). The protofilament diameters, as measured by the distances between V12 C_α sites in the two different molecular layers, are 49 ± 1 Å in Figure 8, panels a and b. The nature of contacts between protofilaments in agitated Aβ_{1-40} fibrils is unknown. Intermolecular salt bridges between K16 and E22 side chains, proposed as possible interactions between protofilaments in our earlier work (*10*), were not detected in subsequent frequency-selective REDOR measurements on agitated Aβ_{1-40} fibrils (*11*). If each individual protofilament has nonzero twist about its long axis, as depicted in Figure 8e, then contacts between protofilaments would vary along the length of the fibril and would not be detectable in our solid-state NMR data. At present, we do not have experimental constraints on the twist of individual protofilaments.

Possibility of Alternative Models. The ratio of structural constraints to amino acid residues in this work is small compared to the analogous ratio in typical structural studies of globular proteins by liquid-state NMR techniques. It is therefore reasonable to ask whether alternative models for Aβ_{1-40} fibril structure might also be consistent with the available constraints. As pointed out previously (*80*), the experimental determination of amyloid structures is greatly simplified by the fact that these structures must be of the cross-β type. In the case of Aβ_{1-40} fibrils, the constraint that the β-strand segments form in-register, parallel β-sheets with cross-β orientation means that relatively few structures are possible once the β-strand segments are identified. MPL data and measurements of fibril dimensions from EM or atomic force microscopy further restrict the number of possible structures. Finally, realistic models must make sense in light of known principles governing the stability of proteins and the fact that the fibrils form in aqueous environments. We have been unable to construct models (even schematically) that are qualitatively different from those in Figure 8 and yet satisfy the same set of experimental constraints.

Given that L17 and F19 reside in the same β-strand and that I32, L34, and V36 reside in the same β-strand, no sets of internal and external quaternary contacts different from those discussed above appear possible. Proximity of I31 and G37, indicated by the data in Figure 5, requires that contacts between the two molecular layers involve the second β-strand. Proximity of side chains of L17 and F19 to side chains of I32, L34, and V36 then requires that these side chains be in the interior of a molecular layer, making internal quaternary contacts. The D23/K28 salt bridge interactions must also occur in the interior of a molecular layer. If the D23/K28 interactions were between different molecular layers, then the C_{2z} symmetry would be lost and only half of the D23 and K28 side chains could participate in these interactions. This would contradict the experimental observation of $\Delta S/S_0$ values greater than 0.5 in Figure 4a. If the D23/K28 interactions were on the exterior of a molecular layer, then we would expect these interactions to be different in hydrated and lyophilized Aβ_{1-40} fibrils. In fact, we have measured indistinguishable REDOR $\Delta S/S_0$ values in hydrated and lyophilized samples.

On the other hand, Aβ_{1-40} fibrils grown under different conditions can have different dimensions, morphologies, MPL values, and NMR spectra, and therefore qualitatively different molecular structures, as we have demonstrated previously for the quiescent and agitated morphologies (*11*) and as reinforced by data in Figure 3. Although we do not yet have full structural models for quiescent Aβ_{1-40} fibrils or for other morphologies, some morphologies may contain the alternative quaternary structures depicted in Figure 1. The alternative structures also appear stable with respect to hydrophobic and electrostatic interactions. MD simulations in explicit solvent support the stability of both C_{2z} and C_{2x}

structures, with both F19/L34 and F19/M35 internal quaternary contacts, on time scales exceeding 10 ns (*76*). The nonspecific nature of hydrophobic interactions, which are apparently the primary stabilizing interactions in Aβ_{1-40} fibrils and in fibrils formed by certain other peptides (*8*, *10*, *37*, *41*), may account for the polymorphism of Aβ_{1-40} fibrils.

Although the models in Figure 8 are consistent with available data for agitated Aβ_{1-40} fibrils, not all aspects of these models are determined uniquely or precisely by the data. For example, available data do not place direct constraints on side chain torsion angles. Backbone torsion angles for residues 22−29 are unconstrained, except by the requirement for D23/K28 interactions and internal quaternary contacts. Thus, the models in Figure 8 are subject to refinement and revision as additional data become available.

Relation to Other Proposed Models for Amyloid Structures. Several early structural models for fibrils formed by full-length β-amyloid peptides assumed antiparallel β-sheets and are therefore inconsistent with current data (*81*−*85*). The models in Figure 8 are similar to our Aβ_{1-40} fibril model published in 2002 (*10*) but differ in the identity of the internal quaternary contacts (F19/L34 in Figure 1b, rather than F19/M35) and the symmetry of the protofilament (C_{2z} rather than C_{2x}). Experimental constraints on internal quaternary contacts and protofilament symmetry were not available when the 2002 model was constructed. In addition, the models in Figure 8 include the intermolecular nature of the internal quaternary contacts and the D23/K28 salt bridge interaction, as supported by the isotopic dilution experiments described above. A model for Aβ_{10-35} fibrils proposed by Ma and Nussinov, also in 2002, has F19/L34 internal quaternary contacts but completely different external contacts (*51*).

A closely related structural model for Aβ_{1-40} fibrils has been proposed by Wetzel and co-workers (*29*, 52), based on proline scanning mutagenesis (*29*), H/D exchange (*27*), and disulfide cross-linking (*52*) experiments, and incorporating the in-register, parallel β-sheet structure established by solid-state NMR (*37*, *38*). In agreement with the models in Figure 8, the model of Wetzel and co-workers places the side chains of L17, F19, I32, L34, and V36 in the interior of a single molecular layer, as supported by the observation of intramolecular disulfide cross-links after oxidation of fibrils formed by L17C/L34C and L17C/V36C double mutants of Aβ_{1-40} (*52*). In contrast to the models in Figure 8, side chains of D23 and K28 are on the exterior of a single molecular layer, and only residues 15−36 are considered to be structurally ordered in the model of Wetzel and co-workers (*29*, *52*). The positions of the D23 and K28 side chains may have been chosen arbitrarily in the model of Wetzel and co-workers. Alternatively, the positions of these side chains may reflect polymorphism, as the D23/K28 salt bridge has been shown to be absent or only partially populated in quiescent Aβ_{1-40} fibrils (*11*) and fibril growth conditions in the experiments of Wetzel and co-workers are not the same as in our solid-state NMR experiments. Disagreement about the extent of structurally ordered segments is likely to arise from differences in the sensitivity of different experimental techniques to disorder. For example, in the site-specific H/D exchange experiments of Whittemore et al. (*27*), backbone amide exchange of roughly 75% or more after a 25 h period at room temperature and pH 7.5 was interpreted as a signature of structural disorder. These data should be viewed in light of H/D exchange measurements on thermostable globular proteins such as protein G_{B2} (*86*), where exchange rates for all backbone amide sites exceed 0.1 h^{-1} at 22 °C and pH 7.0, including all sites in the α-helix and the β-sheet of protein G_{B2}. Exchange rates are expected to increase by a factor of 3.2 at pH 7.5. Thus, while the H/D exchange data of Whittemore et al. on Aβ_{1-40} fibrils do indicate that most residues in segments 15−23 and 27−35 are in highly stable structures, residues outside these segments may be in β-sheets whose stability is comparable to that of protein G_{B2}.

Solid-state ^{13}C NMR line widths suggest that residues 14−16 and 35−40 may be more disordered than residues 10−13 and 17−34, but measurements of intermolecular ^{13}C-^{13}C distances indicate that V12 and V39 are nonetheless in parallel β-sheets (*11*, *38*). Thus, we believe that residues 10−39 in Aβ_{1-40} fibrils are more highly ordered than the N-terminal tail, where larger line widths are observed and intermolecular ^{13}C-^{13}C distances are significantly longer (*11*, *37*, *38*). H/D exchange experiments on Aβ_{1-40} fibrils by Wang et al. (*26*), using exchange periods of 30 min at 25 °C and pH $\approx$ 7.2, indicate that the C-terminal segment is more strongly protected from H/D exchange than the N-terminal segment.

Kajava et al. have proposed a general model for the structure of amyloid fibrils which they call a "parallel superpleated β-structure" (*54*). This model may be considered a generalization of the schematic models in Figure 1a and of our earlier models (*7*, *10*) to higher-molecular-weight systems, such as the amyloid-forming domains of yeast prion proteins (*54*). In a parallel superpleated β-structure, each polypeptide chain adopts a "β-serpentine" conformation, consisting of alternating β-strands and bends, and the β-strands form a stack of in-register, parallel β-sheets. The four-layered β-sheet structures in Figures 1a and 8 resemble the parallel superpleated β-structures envisioned by Kajava et al., except that each Aβ_{1-40} molecule participates in only two β-sheets.

Ritter et al. have proposed a structural model for amyloid fibrils formed by residues 218−289 of the HET-s fungal prion protein (HET-s$_{218-289}$) in which each polypeptide chain participates in two parallel β-sheets but contributes two β-strand segments to each β-sheet (*14*). Unlike the models discussed above, in which all backbone hydrogen bonds between β-strands are intermolecular, half of the backbone hydrogen bonds in the model of Ritter et al. are intramolecular and half are intermolecular. Additional experimental constraints are needed to confirm the model of Ritter et al., but the proposed pattern of backbone hydrogen bonds is supported by the sequence similarity and charge complementarity of pairs of β-strands within HET-s$_{218-289}$ (*14*). Line widths in 2D solid-state ^{13}C-^{13}C NMR spectra of HET-s$_{218-289}$ fibril samples are less than line widths in similar spectra of Aβ_{1-40} fibrils by factors of 3−10, indicating nearly crystalline order in the β-sheets of HET-s$_{218-289}$ fibrils (*14*, *87*). The exceptionally high level of structural order may be a consequence of the fact that the HET-s prion has a clear biological function (*14*, *88*). The amino acid sequence of HET-s$_{218-289}$ does not contain long hydrophobic segments and is not rich in glutamine and asparagine residues, suggesting that the HET-s$_{218-289}$ amyloid structure is stabi-

lized by a specific set of side chain interactions that does not admit the structural variations observed in Aβ_{1-40} fibrils.

Nelson et al. have reported crystal structures of the peptides GNNQQNY and NNQQNY that strongly resemble amyloid structures (*60*). In these crystal structures, each peptide molecule adopts a β-strand conformation and participates in an in-register, parallel β-sheet. Pairs of β-sheets interact through interdigitated side chain−side chain and side chain−backbone contacts. Each pair of β-sheets has C_{2z} symmetry. Thus, the crystal structures of GNNQQNY and NNQQNY have several important features in common with the Aβ_{1-40} fibril models in Figure 8, although the low molecular weight of these peptides prevents a direct comparison of other aspects of symmetry and quaternary interactions.

Finally, several groups have proposed that amyloid fibrils may resemble β-helical proteins (*53*, *85*, *89*, *90*), which contain rodlike helical structures comprised of alternating β-strand and bend segments, with a cross-β orientation of the β-strand segments (*91*). In a β-helical protein, a single polypeptide chain forms multiple turns of the helix. The idealized STAG(+1) and STAG(−1) models in Figure 7 may be considered to be right-handed and left-handed helical structures, respectively, with each Aβ_{1-40} chain forming one turn of the helix, if one links the C-terminus of chain i with the N-terminus of chain i $\pm$ 1. Similarly, if one links the C-terminus of chain i with the N-terminus of chain i $\pm$ 2, the STAG($\pm$2) models may be considered to be helical structures comprised of two intertwined chains. One may then consider the models in Figure 8 to be dimers of β-helices. However, unlike known β-helical proteins, which contain at least three β-strands per turn, each molecular layer in Figure 8 contains two β-strands per turn. The utility of this analogy between the Aβ_{1-40} fibril structure and the structures of β-helical proteins remains to be determined.

REFERENCES

1. Sunde, M., and Blake, C. C. F. (1998) From the globular to the fibrous state: protein structure and structural conversion in amyloid formation, *Q. Rev. Biophys. 31*, 1−39.
2. Tycko, R. (2004) Progress towards a molecular-level structural understanding of amyloid fibrils, *Curr. Opin. Struct. Biol. 14*, 96−103.
3. Caughey, B., and Lansbury, P. T. (2003) Protofibrils, pores, fibrils, and neurodegeneration: Separating the responsible protein aggregates from the innocent bystanders, *Annu. Rev. Neurosci. 26*, 267−298.
4. Wickner, R. B., Edskes, H. K., Ross, E. D., Pierce, M. M., Baxa, U., Brachmann, A., and Shewmaker, F. (2004) Prion genetics: New rules for a new kind of gene, *Annu. Rev. Genet. 38*, 681−707.
5. Chiti, F., Webster, P., Taddei, N., Clark, A., Stefani, M., Ramponi, G., and Dobson, C. M. (1999) Designing conditions for in vitro formation of amyloid protofilaments and fibrils, *Proc. Natl. Acad. Sci. U.S.A. 96*, 3590−3594.
6. Lai, Z. H., Colon, W., and Kelly, J. W. (1996) The acid-mediated denaturation pathway of transthyretin yields a conformational intermediate that can self-assemble into amyloid, *Biochemistry 35*, 6470−6482.
7. Antzutkin, O. N., Leapman, R. D., Balbach, J. J., and Tycko, R. (2002) Supramolecular structural constraints on Alzheimer's β-amyloid fibrils from electron microscopy and solid-state nuclear magnetic resonance, *Biochemistry 41*, 15436−15450.
8. Balbach, J. J. et al. (2000) Amyloid fibril formation by Aβ_{16-22}, a seven-residue fragment of the Alzheimer's β-amyloid peptide, and structural characterization by solid-state NMR, *Biochemistry 39*, 13748−13759.
9. Antzutkin, O. N., Balbach, J. J., and Tycko, R. (2003) Site-specific identification of non-β-strand conformations in Alzheimer's β-amyloid fibrils by solid-state NMR, *Biophys. J. 84*, 3326−3335.
10. Petkova, A. T., Ishii, Y., Balbach, J. J., Antzutkin, O. N., Leapman, R. D., Delaglio, F., and Tycko, R. (2002) A structural model for Alzheimer's β-amyloid fibrils based on experimental constraints from solid-state NMR, *Proc. Natl. Acad. Sci. U.S.A. 99*, 16742−16747.
11. Petkova, A. T., Leapman, R. D., Guo, Z. H., Yau, W. M., Mattson, M. P., and Tycko, R. (2005) Self-propagating, molecular-level polymorphism in Alzheimer's β-amyloid fibrils, *Science 307*, 262−265.
12. Jaroniec, C. P., MacPhee, C. E., Astrof, N. S., Dobson, C. M., and Griffin, R. G. (2002) Molecular conformation of a peptide fragment of transthyretin in an amyloid fibril, *Proc. Natl. Acad. Sci. U.S.A. 99*, 16748−16753.
13. Jaroniec, C. P., MacPhee, C. E., Bajaj, V. S., McMahon, M. T., Dobson, C. M., and Griffin, R. G. (2004) High-resolution molecular structure of a peptide in an amyloid fibril determined by magic angle spinning NMR spectroscopy, *Proc. Natl. Acad. Sci. U.S.A. 101*, 711−716.
14. Ritter, C. et al. (2005) Correlation of structural elements and infectivity of the HET-s prion, *Nature 435*, 844−848.
15. Benzinger, T. L. S., Gregory, D. M., Burkoth, T. S., Miller-Auer, H., Lynn, D. G., Botto, R. E., and Meredith, S. C. (2000) Two-dimensional structure of β-amyloid(10−35) fibrils, *Biochemistry 39*, 3491−3499.
16. Gregory, D. M., Benzinger, T. L. S., Burkoth, T. S., Miller-Auer, H., Lynn, D. G., Meredith, S. C., and Botto, R. E. (1998) Dipolar recoupling NMR of biomolecular self-assemblies: determining inter- and intrastrand distances in fibrilized Alzheimer's β-amyloid peptide, *Solid State Nucl. Magn. Reson. 13*, 149−166.
17. Heller, J. et al. (1996) Solid-state NMR studies of the prion protein H1 fragment, *Protein Sci. 5*, 1655−1661.
18. Laws, D. D. et al. (2001) Solid-state NMR studies of the secondary structure of a mutant prion protein fragment of 55 residues that induces neurodegeneration, *Proc. Natl. Acad. Sci. U.S.A. 98*, 11686−11690.
19. Naito, A., Kamihira, M., Inoue, R., and Saito, H. (2004) Structural diversity of amyloid fibril formed in human calcitonin as revealed by site-directed ^{13}C solid-state NMR spectroscopy, *Magn. Reson. Chem. 42*, 247−257.
20. Kheterpal, I., Zhou, S., Cook, K. D., and Wetzel, R. (2000) Aβ amyloid fibrils possess a core structure highly resistant to hydrogen exchange, *Proc. Natl. Acad. Sci. U.S.A. 97*, 13597−13601.
21. Hoshino, M., Katou, H., Hagihara, Y., Hasegawa, K., Naiki, H., and Goto, Y. (2002) Mapping the core of the β_2-microglobulin amyloid fibril by H/D exchange, *Nat. Struct. Biol. 9*, 332−336.
22. Ippel, J. H., Olofsson, A., Schleucher, J., Lundgren, E., and Wijmenga, S. S. (2002) Probing solvent accessibility of amyloid fibrils by solution NMR spectroscopy, *Proc. Natl. Acad. Sci. U.S.A. 99*, 8648−8653.
23. Kuwata, K., Matumoto, T., Cheng, H., Nagayama, K., James, T. L., and Roder, H. (2003) NMR-detected hydrogen exchange and molecular dynamics simulations provide structural insight into fibril formation of prion protein fragment 106−126, *Proc. Natl. Acad. Sci. U.S.A. 100*, 14790−14795.
24. Yamaguchi, K. I., Katou, H., Hoshino, M., Hasegawa, K., Naiki, H., and Goto, Y. (2004) Core and heterogeneity of β_2-microglobulin amyloid fibrils as revealed by H/D exchange, *J. Mol. Biol. 338*, 559−571.
25. Olofsson, A., Ippel, J. H., Wijmenga, S. S., Lundgren, E., and Ohman, A. (2004) Probing solvent accessibility of transthyretin amyloid by solution NMR spectroscopy, *J. Biol. Chem. 279*, 5699−5707.
26. Wang, S. S. S., Tobler, S. A., Good, T. A., and Fernandez, E. J. (2003) Hydrogen exchange-mass spectrometry analysis of β-amyloid peptide structure, *Biochemistry 42*, 9507−9514.
27. Whittemore, N. A., Mishra, R., Kheterpal, I., Williams, A. D., Wetzel, R., and Serpersu, E. H. (2005) Hydrogen−deuterium (H/D) exchange mapping of Aβ(1−40) amyloid fibril secondary structure using nuclear magnetic resonance spectroscopy, *Biochemistry 44*, 4434−4441.
28. Thakur, A. K., and Wetzel, R. (2002) Mutational analysis of the structural organization of polyglutamine aggregates, *Proc. Natl. Acad. Sci. U.S.A. 99*, 17014−17019.
29. Williams, A. D., Portelius, E., Kheterpal, I., Guo, J. T., Cook, K. D., Xu, Y., and Wetzel, R. (2004) Mapping Aβ amyloid fibril

secondary structure using scanning proline mutagenesis, *J. Mol. Biol. 335*, 833−842.
30. Jayasinghe, S. A., and Langen, R. (2004) Identifying structural features of fibrillar islet amyloid polypeptide using site-directed spin labeling, *J. Biol. Chem. 279*, 48420−48425.
31. Der-Sarkissian, A., Jao, C. C., Chen, J., and Langen, R. (2003) Structural organization of α-synuclein fibrils studied by site-directed spin labeling, *J. Biol. Chem. 278*, 37530−37535.
32. Torok, M., Milton, S., Kayed, R., Wu, P., McIntire, T., Glabe, C. G., and Langen, R. (2002) Structural and dynamic features of Alzheimer's Aβ peptide in amyloid fibrils studied by site-directed spin labeling, *J. Biol. Chem. 277*, 40810−40815.
33. Fraser, P. E., Nguyen, J. T., Inouye, H., Surewicz, W. K., Selkoe, D. J., Podlisny, M. B., and Kirschner, D. A. (1992) Fibril formation by primate, rodent, and Dutch-hemorrhagic analogs of Alzheimer amyloid β-protein, *Biochemistry 31*, 10716−10723.
34. Dong, J., Atwood, C. S., Anderson, V. E., Siedlak, S. L., Smith, M. A., Perry, G., and Carey, P. R. (2003) Metal binding and oxidation of amyloid-β within isolated senile plaque cores: Raman microscopic evidence, *Biochemistry 42*, 2768−2773.
35. Lansbury, P. T. et al. (1995) Structural model for the β-amyloid fibril based on interstrand alignment of an antiparallel sheet comprising a C-terminal peptide, *Nat. Struct. Biol. 2*, 990−998.
36. Benzinger, T. L. S., Gregory, D. M., Burkoth, T. S., Miller-Auer, H., Lynn, D. G., Botto, R. E., and Meredith, S. C. (1998) Propagating structure of Alzheimer's β-amyloid$_{10-35}$ is parallel β-sheet with residues in exact register, *Proc. Natl. Acad. Sci. U.S.A. 95*, 13407−13412.
37. Antzutkin, O. N., Balbach, J. J., Leapman, R. D., Rizzo, N. W., Reed, J., and Tycko, R. (2000) Multiple quantum solid-state NMR indicates a parallel, not antiparallel, organization of β-sheets in Alzheimer's β-amyloid fibrils, *Proc. Natl. Acad. Sci. U.S.A. 97*, 13045−13050.
38. Balbach, J. J., Petkova, A. T., Oyler, N. A., Antzutkin, O. N., Gordon, D. J., Meredith, S. C., and Tycko, R. (2002) Supramolecular structure in full-length Alzheimer's β-amyloid fibrils: Evidence for a parallel β-sheet organization from solid-state nuclear magnetic resonance, *Biophys. J. 83*, 1205−1216.
39. Tycko, R., and Ishii, Y. (2003) Constraints on supramolecular structure in amyloid fibrils from two-dimensional solid-state NMR spectroscopy with uniform isotopic labeling, *J. Am. Chem. Soc. 125*, 6606−6607.
40. Gordon, D. J., Balbach, J. J., Tycko, R., and Meredith, S. C. (2004) Increasing the amphiphilicity of an amyloidogenic peptide changes the β-sheet structure in the fibrils from antiparallel to parallel, *Biophys. J. 86*, 428−434.
41. Petkova, A. T., Buntkowsky, G., Dyda, F., Leapman, R. D., Yau, W. M., and Tycko, R. (2004) Solid-state NMR reveals a pH-dependent antiparallel β-sheet registry in fibrils formed by a β-amyloid peptide, *J. Mol. Biol. 335*, 247−260.
42. Chan, J. C. C., Oyler, N. A., Yau, W. M., and Tycko, R. (2005) Parallel β-sheets and polar zippers in amyloid fibrils formed by residues 10−39 of the yeast prion protein Ure2p, *Biochemistry 44*, 10669−10680.
43. Sciarretta, K. L., Gordon, D. J., Petkova, A. T., Tycko, R., and Meredith, S. C. (2005) Aβ 40-Lactam(D23/K28) models a conformation highly favorable for nucleation of amyloid, *Biochemistry 44*, 6003−6014.
44. Kammerer, R. A. et al. (2004) Exploring amyloid formation by a *de novo* design, *Proc. Natl. Acad. Sci. U.S.A. 101*, 4435−4440.
45. Margittai, M., and Langen, R. (2004) Template-assisted filament growth by parallel stacking of tau, *Proc. Natl. Acad. Sci. U.S.A. 101*, 10278−10283.
46. Serag, A. A., Altenbach, C., Gingery, M., Hubbell, W. L., and Yeates, T. O. (2002) Arrangement of subunits and ordering of β-strands in an amyloid sheet, *Nat. Struct. Biol. 9*, 734−739.
47. Astbury, W. T., Dickinson, S., and Bailey, K. (1935) The X-ray interpretation of denaturation and the structure of the seed globulins, *Biochem. J. 29*, 2351.
48. Eanes, E. D., and Glenner, G. G. (1968) X-ray diffraction studies on amyloid filaments, *J. Histochem. Cytochem. 16*, 673−677.
49. Serpell, L. C., and Smith, J. M. (2000) Direct visualisation of the β-sheet structure of synthetic Alzheimer's amyloid, *J. Mol. Biol. 299*, 225−231.
50. Oyler, N. A., and Tycko, R. (2004) Absolute structural constraints on amyloid fibrils from solid state NMR spectroscopy of partially oriented samples, *J. Am. Chem. Soc. 126*, 4478−4479.
51. Ma, B. Y., and Nussinov, R. (2002) Stabilities and conformations of Alzheimer's β-amyloid peptide oligomers (Aβ_{16-22}, Aβ_{16-35}, and Aβ_{10-35}): Sequence effects, *Proc. Natl. Acad. Sci. U.S.A. 99*, 14126−14131.
52. Shivaprasad, S., and Wetzel, R. (2004) An intersheet packing interaction in Aβ fibrils mapped by disulfide cross-linking, *Biochemistry 43*, 15310−15317.
53. Guo, J. T., Wetzel, R., and Ying, X. (2004) Molecular modeling of the core of Aβ amyloid fibrils, *Proteins 57*, 357−364.
54. Kajava, A. V., Baxa, U., Wickner, R. B., and Steven, A. C. (2004) A model for Ure2p prion filaments and other amyloids: The parallel superpleated β-structure, *Proc. Natl. Acad. Sci. U.S.A. 101*, 7885−7890.
55. Kajava, A. V., Aebi, U., and Steven, A. C. (2005) The parallel superpleated β-structure as a model for amyloid fibrils of human amylin, *J. Mol. Biol. 348*, 247−252.
56. Jimenez, J. L., Guijarro, J. L., Orlova, E., Zurdo, J., Dobson, C. M., Sunde, M., and Saibil, H. R. (1999) Cryo-electron microscopy structure of an SH3 amyloid fibril and model of the molecular packing, *EMBO J. 18*, 815−821.
57. Jimenez, J. L., Nettleton, E. J., Bouchard, M., Robinson, C. V., Dobson, C. M., and Saibil, H. R. (2002) The protofilament structure of insulin amyloid fibrils, *Proc. Natl. Acad. Sci. U.S.A. 99*, 9196−9201.
58. Burkoth, T. S. et al. (2000) Structure of the β-amyloid$_{10-35}$ fibril, *J. Am. Chem. Soc. 122*, 7883−7889.
59. Makin, O. S., Atkins, E., Sikorski, P., Johansson, J., and Serpell, L. C. (2005) Molecular basis for amyloid fibril formation and stability, *Proc. Natl. Acad. Sci. U.S.A. 102*, 315−320.
60. Nelson, R., Sawaya, M. R., Balbirnie, M., Madsen, A. O., Riekel, C., Grothe, R., and Eisenberg, D. (2005) Structure of the cross-β spine of amyloid-like fibrils, *Nature 435*, 773−778.
61. Roher, A. E. et al. (1993) Structural alterations in the peptide backbone of β-amyloid core protein may account for its deposition and stability in Alzheimer's disease, *J. Biol. Chem. 268*, 3072−3083.
62. Kheterpal, I., Williams, A., Murphy, C., Bledsoe, B., and Wetzel, R. (2001) Structural features of the Aβ amyloid fibril elucidated by limited proteolysis, *Biochemistry 40*, 11757−11767.
63. Bennett, A. E., Rienstra, C. M., Auger, M., Lakshmi, K. V., and Griffin, R. G. (1995) Heteronuclear decoupling in rotating solids, *J. Chem. Phys. 103*, 6951−6958.
64. Raleigh, D. P., Levitt, M. H., and Griffin, R. G. (1988) Rotational resonance in solid-state NMR, *Chem. Phys. Lett. 146*, 71−76.
65. Takegoshi, K., Nakamura, S., and Terao, T. (2001) ^{13}C−^{1}H dipolar-assisted rotational resonance in magic-angle spinning NMR, *Chem. Phys. Lett. 344*, 631−637.
66. Morcombe, C. R., Gaponenko, V., Byrd, R. A., and Zilm, K. W. (2004) Diluting abundant spins by isotope edited radio frequency field assisted diffusion, *J. Am. Chem. Soc. 126*, 7196−7197.
67. Gullion, T., and Schaefer, J. (1989) Rotational echo double resonance NMR, *J. Magn. Reson. 81*, 196−200.
68. Jaroniec, C. P., Tounge, B. A., Herzfeld, J., and Griffin, R. G. (2001) Frequency selective heteronuclear dipolar recoupling in rotating solids: Accurate ^{13}C-^{15}N distance measurements in uniformly ^{13}C,^{15}N-labeled peptides, *J. Am. Chem. Soc. 123*, 3507−3519.
69. Jaroniec, C. P., Filip, C., and Griffin, R. G. (2002) 3D TEDOR NMR experiments for the simultaneous measurement of multiple carbon−nitrogen distances in uniformly ^{13}C,^{15}N-labeled solids, *J. Am. Chem. Soc. 124*, 10728−10742.
70. Michal, C. A., and Jelinski, L. W. (1997) REDOR 3D: Heteronuclear distance measurements in uniformly labeled and natural abundance solids, *J. Am. Chem. Soc. 119*, 9059−9060.
71. Hing, A. W., Vega, S., and Schaefer, J. (1992) Transferred echo double resonance NMR, *J. Magn. Reson. 96*, 205−209.
72. Wishart, D. S. et al. (1995) ^{1}H, ^{13}C and ^{15}N chemical shift referencing in biomolecular NMR, *J. Biomol. NMR 6*, 135−140.
73. Koradi, R., Billeter, M., and Wuthrich, K. (1996) MOLMOL: A program for display and analysis of macromolecular structures, *J. Mol. Graph. 14*, 51−55.
74. Gorbitz, C. H. (2000) An NH_3^+···phenyl interaction in L-phenylalanyl-L-valine, *Acta Crystallogr. Sect. C−Cryst. Struct. Commun. 56*, 1496−1498.
75. Castellani, F., van Rossum, B. J., Diehl, A., Rehbein, K., and Oschkinat, H. (2003) Determination of solid-state NMR structures of proteins by means of three-dimensional ^{15}N-^{13}C-^{13}C dipolar correlation spectroscopy and chemical shift analysis, *Biochemistry 42*, 11476−11483.

76. Buchete, N.-V., Tycko, R., and Hummer, G. (2005) Molecular dynamics simulations of Alzheimer's β-amyloid protofilaments, *J. Mol. Biol. 353*, 804−821.
77. Hou, L. M., Kang, I., Marchant, R. E., and Zagorski, M. G. (2002) Methionine-35 oxidation reduces fibril assembly of the amyloid Aβ_{1-42} peptide of Alzheimer's disease, *J. Biol. Chem. 277*, 40173−40176.
78. Riek, R., Guntert, P., Dobeli, H., Wipf, B., and Wuthrich, K. (2001) NMR studies in aqueous solution fail to identify significant conformational differences between the monomeric forms of two Alzheimer peptides with widely different plaque-competence, Aβ_{1-40}(ox) and Aβ_{1-42}(ox), *Eur. J. Biochem. 268*, 5930−5936.
79. Bitan, G., Tarus, B., Vollers, S. S., Lashuel, H. A., Condron, M. M., Straub, J. E., and Teplow, D. B. (2003) A molecular switch in amyloid assembly: Met35 and amyloid β-protein oligomerization, *J. Am. Chem. Soc. 125*, 15359−15365.
80. Tycko, R. (2003) Insights into the amyloid folding problem from solid-state NMR, *Biochemistry 42*, 3151−3159.
81. George, A. R., and Howlett, D. R. (1999) Computationally derived structural models of the β-amyloid found in Alzheimer's disease plaques and the interaction with possible aggregation inhibitors, *Biopolymers 50*, 733−741.
82. Chaney, M. O., Webster, S. D., Kuo, Y. M., and Roher, A. E. (1998) Molecular modeling of the Aβ_{1-42} peptide from Alzheimer's disease, *Protein Eng. 11*, 761−767.
83. Li, L. P., Darden, T. A., Bartolotti, L., Kominos, D., and Pedersen, L. G. (1999) An atomic model for the pleated β-sheet structure of Aβ amyloid protofilaments, *Biophys. J. 76*, 2871−2878.
84. Tjernberg, L. O. et al. (1999) A molecular model of Alzheimer amyloid β-peptide fibril formation, *J. Biol. Chem. 274*, 12619−12625.
85. Lazo, N. D., and Downing, D. T. (1998) Amyloid fibrils may be assembled from β-helical protofibrils, *Biochemistry 37*, 1731−1735.
86. Orban, J., Alexander, P., and Bryan, P. (1994) Hydrogen−deuterium exchange in the free and immunoglobulin G-bound protein-G B-domain, *Biochemistry 33*, 5702−5710.
87. Siemer, A. B., Ritter, C., Ernst, M., Riek, R., and Meier, B. H. (2005) High-resolution solid-state NMR spectroscopy of the prion protein HET-s in its amyloid conformation, *Angew. Chem., Int. Ed. 44*, 2441−2444.
88. Coustou, V., Deleu, C., Saupe, S., and Begueret, J. (1997) The protein product of the het-s heterokaryon incompatibility gene of the fungus *Podospora anserina* behaves as a prion analog, *Proc. Natl. Acad. Sci. U.S.A. 94*, 9773−9778.
89. Govaerts, C., Wille, H., Prusiner, S. B., and Cohen, F. E. (2004) Evidence for assembly of prions with left-handed β_3-helices into trimers, *Proc. Natl. Acad. Sci. U.S.A. 101*, 8342−8347.
90. Perutz, M. F., Finch, J. T., Berriman, J., and Lesk, A. (2002) Amyloid fibers are water-filled nanotubes, *Proc. Natl. Acad. Sci. U.S.A. 99*, 5591−5595.
91. Jenkins, J., and Pickersgill, R. (2001) The architecture of parallel β-helices and related folds, *Prog. Biophys. Mol. Biol. 77*, 111−175.

BI051952Q